Predictability of the Western North Pacific Subtropical High Associated with Different ENSO Phases in GloSea5

Daquan ZHANG[1*], Gill M. MARTIN[2], José M. RODRÍGUEZ[2], Zongjian KE[1], and Lijuan CHEN[1]

1 *Laboratory for Climate Studies*, *National Climate Center*, *China Meteorological Administration*, *Beijing* 100081, *China*
2 *Met Office Hadley Centre, Exeter* EX1 3PB, *UK*

(Received March 25, 2020; in final form July 26, 2020)

ABSTRACT

The western North Pacific subtropical high (WNPSH) dominates the summer climate over East Asia. The intensity, position, and shape of WNPSH influence the spatiotemporal distributions of precipitation, temperature, and tropical cyclone activities in this region. This paper intends to investigate the performance of the UK Met Office Global Seasonal forecast system version 5 (GloSea5) in simulation/prediction of the WNPSH based on a hindcast dataset. Analyses of the hindcast data show a systematic bias in the mean circulation over West Pacific, with negative geopotential height anomalies over the western North Pacific (WNP) and cyclonic anomalies in the 850-hPa winds and water vapor transport, indicating a weakening and eastward shift of the WNPSH. Despite the model's bias in the climatology, it well captured the interannual variability of the monthly and seasonal-mean intensity of the WNPSH and the position of its ridge line in boreal summer from 1993 to 2015. The seasonal hindcasts indicate that there is significant prediction skill at up to three-month lead time for both the intensity and position of the WNPSH ridge line. The relationship between the WNPSH and different phases of the El Niño–Southern Oscillation (ENSO) in both the observational data and GloSea5 hindcasts was then investigated. The model captured the summer WNPSH anomalies well during most of the ENSO phases, except in the La Niña decaying and neutral summers. The intensity of the anticyclone in the WNP is weak in the decaying phase of El Niño in the GloSea5 hindcasts compared with the reanalysis data. GloSea5 is capable of representing the lagged teleconnection between El Niño events in the previous winter and the intensity of the WNPSH in the following summer. Regression analysis reveals weakened negative sea surface temperature anomalies (SSTAs) over the WNP in GloSea5, which reduced the gradient between the tropical western Pacific and the tropical Indian Ocean, resulting in a weaker easterly anomaly and stronger westerly anomaly, contributing to the weak anomalous anticyclone over the WNP and the weakened WNPSH relative to the reanalysis data.

Key words: western North Pacific subtropical high (WNPSH), Global Seasonal forecast system version 5 (GloSea5), El Niño–Southern Oscillation (ENSO), precipitation, predictability

Citation: Zhang, D. Q., G. M. Martin, J. M. Rodríguez, et al., 2020: Predictability of the western North Pacific subtropical high associated with different ENSO phases in GloSea5. *J. Meteor. Res.*, **34**(5), 926–940, doi: 10.1007/s13351-020-0055-1.

1. Introduction

The western North Pacific subtropical high (WNPSH) is an important component of the East Asian monsoon (EAM) system. The position, shape, and strength of the WNPSH dominate the large-scale quasi-stationary frontal zones of the EAM (Tao et al., 2001; Lee et al., 2006). The low-level jet on its northwest flank transports a large amount of water vapor into the mid and high latitudes of East Asia (Niñomiya and Kobayashi, 1998, 1999; Lu and Dong, 2001). The intraseasonal variability of the WNPSH from late spring to summer leads to northward jumps of the main rain belt in East China, which corresponds to the beginning of the pre-flood season in South China, the Meiyu season in the Yangtze and Huai River valleys (Liu et al., 2013), and the rainy season in North

Supported by the National Key Research and Development Program of China (2017YFC1502303), National Natural Science Fundation of China (41730964, 41975091, and 41605078), and UK–China Research and Innovation Partnership Fund through the Met Office Climate Science for Service Partnership (CSSP) China as part of the Newton Fund.

*Corresponding author: zhangdq@cma.gov.cn.

and Northeast China. The WNPSH also shows a substantial interannual variability. Its intensity and position are closely related to the spatial patterns of summer rainfall in China (Yuan et al., 2016). In addition to its significant impact on rainfall over the EAM region, the WNPSH has a profound effect on heat waves (Hong et al., 2018; Chen et al., 2019) and tropical storm activity in the western North Pacific (WNP; Wang et al., 2013).

The interannual variation in the WNPSH is closely related to the thermal state of the tropical oceans, particularly that associated with the El Niño–Southern Oscillation (ENSO; Wang et al., 2000; Wang and Zhang, 2002; Chou et al., 2003; Wu and Zhou, 2008; Li et al., 2012, 2014; Xue et al., 2018). The intensity and position of the WNPSH in summer have a close relationship with El Niño events in boreal winter two seasons earlier. The appearance of an anticyclonic anomaly to the north of the Maritime Continent in the lower troposphere during the mature phase of the El Niño intensifies the WNPSH and shifts it westward (Zhang et al., 1999). Observational analysis has shown that the central and eastern tropical Pacific (CEP) and central tropical Indian Ocean (TIO) are two key regions that affect the variations in the WNPSH in summer (Yun et al., 2013; Qian et al., 2018). During the mature phase of El Niño events in boreal winter, warm sea surface temperature anomalies (SSTAs) in CEP affect the WNPSH through the anomalous Walker circulation and the associated low-level anticyclone near the Philippines (Yuan et al., 2012). In the subsequent spring and summer, as a lagged response to the Pacific SSTAs, the warm SSTAs in TIO play an important part in maintenance of the anticyclone near the Philippines, contributing to the intensification of the WNPSH. Xie et al. (2009, 2016) synthesized the wind–evaporation–sea surface temperature (SST) feedback mechanism and the SSTA warming in the westerly monsoon regime of the northern Indian Ocean, proposing the Indo–western Pacific Ocean capacitor effect, which emphasizes the role of the Indian Ocean in the persistent influence of the ENSO on the climate of East Asia. Nevertheless, the relative contributions of the Indian Ocean and the tropical Pacific SSTAs to the variability of the WNPSH and associated representative ability of dynamic models are not yet clear.

Previous studies have shown the robust predictive skill of the UK Met Office Global Seasonal forecast system version 5 (GloSea5) for tropical cyclones over the WNP (Camp et al., 2015), the onset of the summer monsoon in the South China Sea (Martin et al., 2019), wind speeds in winter (Lockwood et al., 2019), seasonal rainfall in the Yangtze River valley (Li et al., 2016; Bett et al., 2017) and South China (Lu et al., 2017), June rainfall in the mid to lower Yangtze River valley (Martin et al., 2020), and the asymmetrical response of the EAM to El Niño and La Niña events (Hardiman et al., 2018). Simulation and prediction of the WNPSH, a key component of the EAM system, are important for both seasonal and subseasonal climate predictions. In this paper, we aim to investigate the simulation and prediction skill of the WNPSH and its relationship with the ENSO and Indian Ocean SSTAs in the operational hindcast dataset of the UK Met Office GloSea5 seasonal forecasting system.

The remainder of this paper is organized as follows. Section 2 presents the model, data, and methods. Section 3 shows the systematic bias of the WNPSH in both the atmospheric-only free-running and GloSea5 hindcast datasets, including the monthly and seasonal forecast skills of the WNPSH intensity and the latitudinal position of the ridge line. Section 4 discusses the predictability of the WNPSH and its relationship to the tropical Pacific and Indian oceans, especially under the background of different phases of ENSO. A summary as well as discussion is presented in Section 5.

2. Models, hindcast experiments, and observations

The UK Met Office GloSea5 model (MacLachlan et al., 2015) is based on the Global Coupled 2 (GC2) configuration of the Met Office Hadley Centre Global Environment Model version 3 (HadGEM3; Williams et al., 2015), which couples the Met Office Unified Model (MetUM) atmosphere component Global Atmosphere 6 (GA6; Walters et al., 2017), the Joint UK Land Environment Simulator (JULES; Best et al., 2011), the Nucleus for European Modelling of the Ocean (NEMO; Megann et al., 2014), and the Los Alamos sea ice model (CICE; Rae et al., 2015) using the Ocean Atmosphere Sea Ice Soil (OASIS) coupler (Valcke, 2013). GloSea5 uses the N216L85 version (0.83° latitude × 0.56° longitude, with 85 vertical levels reaching a height of 85 km near the mesopause) for the atmosphere and a 0.25° horizontal grid and 75 quasi-horizontal levels in the ocean (0.25L75). All climate forcings (e.g., aerosols and carbon dioxide concentrations) are set to observed values, and the model contains no flux correction or relaxation to the climatology.

We used an atmosphere-only climate configuration of Global Atmosphere 7 (GA7; Walters et al., 2019) to study the mean state of the WNPSH and associated moisture transport in the EAM region. Compared with the GA6 atmosphere component used in GC2, GA7 includes

changes to both the model physics and dynamics, several of which were designed to tackle critical model errors. The integrations were produced with the same surface temperature, sea ice, and other external forcing as the Coupled Model Intercomparison Project Phase 5 (CMIP5). The simulations will be referred to as MetUM hereafter. Retrospective forecasts in GloSea5 were produced to evaluate the skill of the system in forecasting for the boreal summer (June–August) initialized on 1st, 9th, 17th, and 25th of March, April, and May from 1993 to 2015. Each start date has 7 ensemble members, with the ensemble spread provided by using a stochastic kinetic energy backscatter scheme (SKEB2; Bowler et al., 2009), and thus, the ensemble mean from each month has a total of 28 members.

The latest released ECWMF fifth-generation reanalysis product (ERA5) was used to evaluate the climatology and variability of the atmospheric circulation associated with the WNPSH and to assess model simulations in the EAM region. The ERA5 reanalysis product has a better evaluation applicability in the relative humidity and wind fields, especially in the lower layers of the troposphere (Hoffmann et al., 2019), than ERA-Interim (Dee et al., 2011). The Global Precipitation Climatology Project (GPCP) version 2.3 monthly precipitation dataset was used to evaluate the GloSea5 rainfall in summer (Adler et al., 2018). The version 2.3 monthly data used cover the period from 1979 to the present day and provide a consistent analysis of global precipitation from the integration of various satellite datasets for the land and oceans and a gauge analysis over land. SST observations are taken from the Hadley Centre Global Sea Ice and Sea Surface Temperature (HadISST; Rayner et al., 2003). For convenience, we refer to these observation-based datasets as observations.

3. Simulation and prediction of WNPSH

3.1 *Climatology*

The 500-hPa geopotential height has been widely used in real-time monitoring of the WNPSH (Lu et al., 2008; He et al., 2018). For example, the China Meteorological Administration defined the WNPSH area and intensity indices using the 5880-gpm contour lines in the 500-hPa geopotential height fields (Liu et al., 2012). Figure 1 shows the climatological bias of the geopotential height at 500 hPa and horizontal winds at 850 hPa for the EAM region in both the MetUM atmosphere-only free-running simulation and the ensemble mean of the GloSea5 hindcasts initialized on start dates in May. The model shows a weak WNPSH in June, July, and August (JJA) compared with the reanalysis results, and the negative bias tends to intensify with longer lead times, especially in GloSea5. In August, the WNPSH simulated by GloSea5 is so weak that the 5860-gpm contour disappears (Fig. 1i). The simulated horizontal 850-hPa wind field is closest to the observations in June.

There are stronger westerly winds over the South China Sea and the Philippines, and a negative bias in the 500-hPa geopotential height over the WNP region, resulting in an eastward shift of WNPSH in GloSea5. The spatial patterns for the climatological bias of atmospheric circulation over the WNP of the GloSea5 hindcast initialized from March and April are similar (figures omitted). The negative bias of the geopotential height over the WNP is more significant in March than in April and May, indicating a trend of decreased bias with a shorter lead time. The negative bias of geopotential height over the WNP region and stronger westerly winds are more significant than in the MetUM simulation, suggesting that the bias is strengthened with the atmosphere–ocean coupling.

Figure 2 shows the vertically integrated moisture flux and precipitation from the ERA5/GPCP data and the climatological bias of the MetUM and GloSea5 simulations. As a deep circulation system located in the mid and lower troposphere (Gao et al., 2017), the WNPSH and its simulated climatological bias are highly correlated with the summer rainfall over East Asia. The weakening and eastward displacement of WNPSH shows a negative bias in the 500-hPa geopotential height field and the cyclonic anomalies of wind fields over the WNP region. The cyclonic wind anomalies deepen the monsoon trough and promote strengthening of the monsoon flow and moisture transport on its southern side, contributing to the positive rainfall bias to the east of the Philippines. The cyclonic bias in the wind field in both the MetUM and GloSea5 hindcasts leads to the weakened transport of moisture to East China, which results in a negative bias in the precipitation. Aligned with the subseasonal northward movement of the main rain belt of the monsoon in East China, the negative bias also shows a north-moving trend from June to August, while a positive bias is seen in South and Southwest China.

The ridge-line latitude is used to denote the meridional location of the WNPSH, which is defined by the meridional mean of the latitudinal position of the isoline where the 500-hPa zonal wind $u = 0$ and $\partial u/\partial y > 0$ surrounded by the 5880-gpm contour (Liu et al., 2012, 2014) between 110° and 160°E. The major bias is a northward displacement of the WNPSH ridge line in both the GA7 simulation and the GloSea5 hindcasts, which is also a

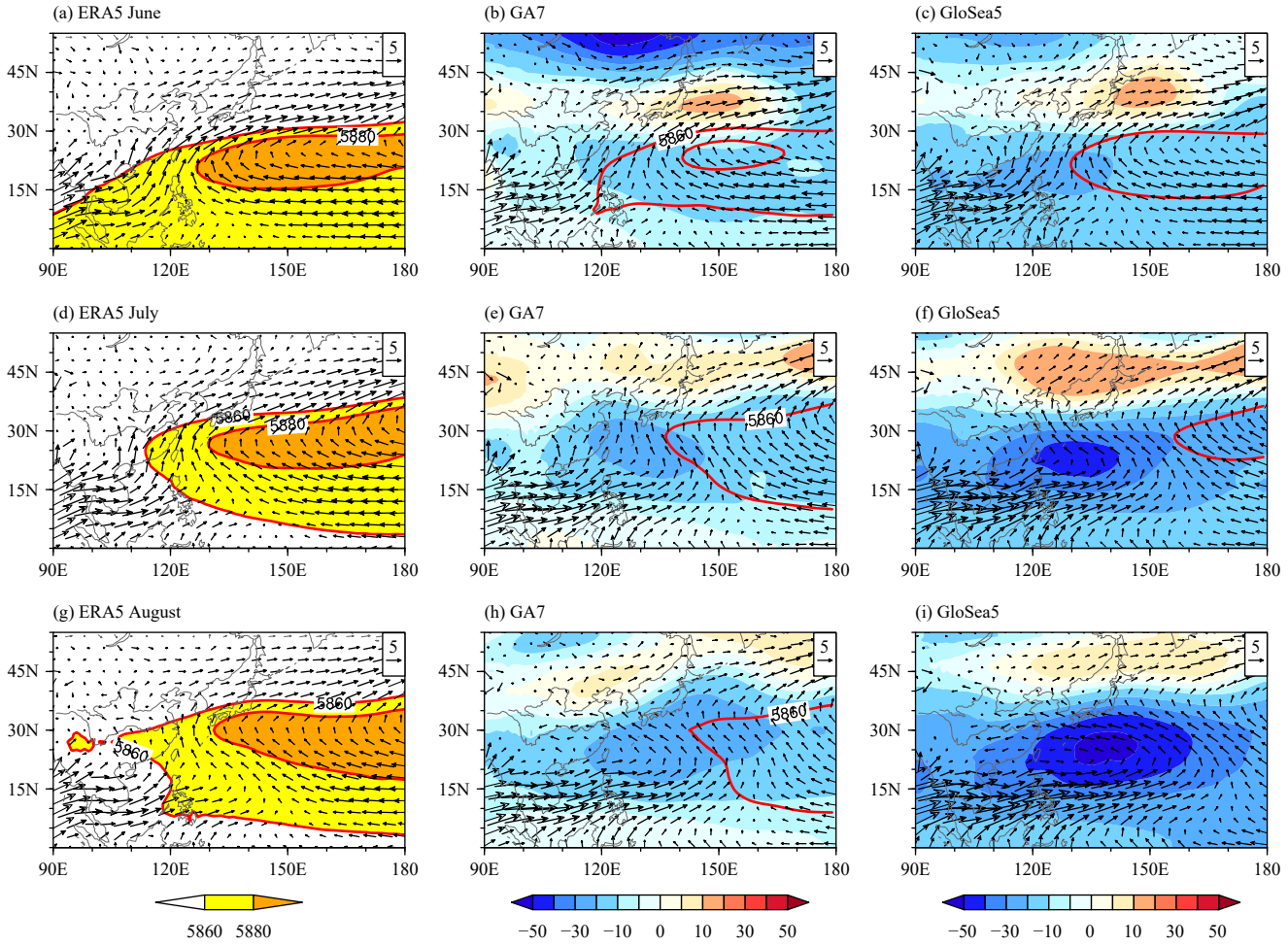

Fig. 1. Climatological geopotential height at 500 hPa (red contour; gpm) and horizontal winds at 850 hPa (vector; m s^{-1}) from (a, d, g) observations (ERA5), (b, e, h) MetUM atmosphere-only (GA7) free-running simulation, and (c, f, i) GloSea5 hindcasts (with start dates in May), for (a–c) June, (d–f) July, and (g–i) August. Shadings in (a, d, g) denote observational climatology, while in (b, e, h) and (c, f, i) denote model bias. Red bold lines denote the 5880- and 5860-gpm isolines.

common bias among the CMIP5 models (He and Zhou, 2014). Figure 3 shows that the climatological latitudinal position of the WNPSH ridge line in GA7 moves northward relative to the ERA5 results. In August, the ridge line is located outside the 5880-gpm contour and is therefore not shown. For the GloSea5 hindcasts, there is a systematic bias of a northward displacement of 1°–2° latitudes in July and August, but good agreement with the observations in June, which might contribute to the relatively high prediction skill of the June-mean rainfall in the mid and lower Yangtze River basin (Martin et al., 2020). Corresponding to the northward displacement of the WNPSH, the monsoon trough is stronger and the Meiyu–Baiu rain belt is weaker than in the observations.

3.2 *Interannual variation*

Figure 4 shows seasonal prediction of the intensity of WNPSH (Wang et al., 2013) and the position of its ridge line in JJA in GloSea5. The correlation coefficient for the intensity of WNPSH is 0.75 between GloSea5 and reanalysis dataset (ERA5) with a three-month lead time (defined here for all start dates in March), consistent with the results of MacLachlan et al. (2015). As the lead time decreases, the correlation coefficients show an upward trend, with 0.84 for the forecast initialized in May. For the years with a strong El Niño event in the previous winter, the intensity of WNPSH in GloSea5 hindcasts is very close to the observations. Monthly results from the hindcast also show considerable prediction skill, with the prediction skill for the WNPSH intensity in JJA with a start date in May of 0.71, 0.64, and 0.65, respectively. The prediction skill decreases with the increasing lead time of the forecast. However, among the predictions with start dates in April and March, the best forecast performance is for July, with a correlation coefficient of 0.70 (Table 1). The possible mechanism for the relat-

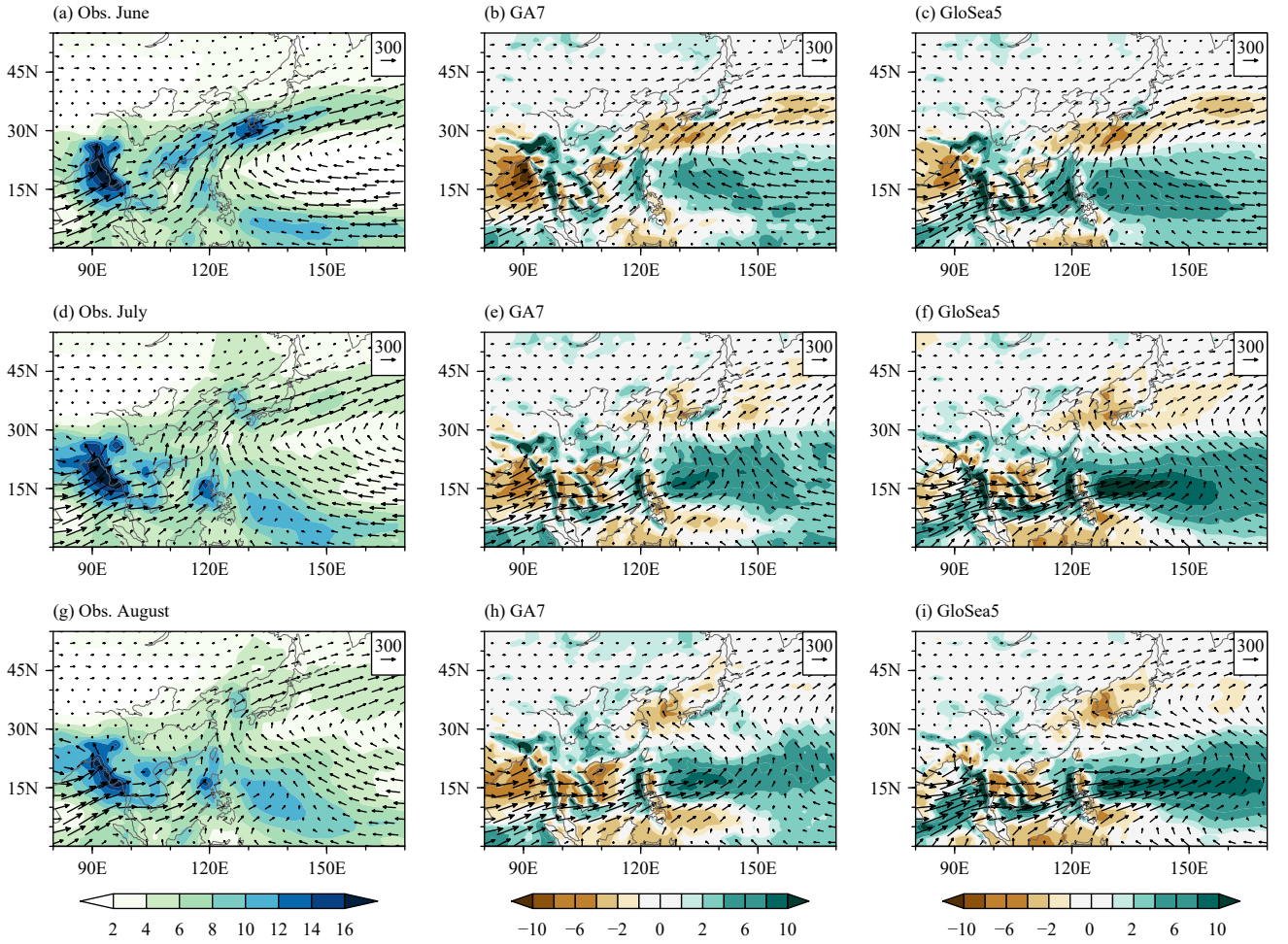

Fig. 2. Vertically integrated moisture flux (vector; m s^{-1}) and precipitation (shading; mm day^{-1}) from (a, d, g) observations (ERA moisture flux and GPCP precipitation), (b, e, h) MetUM atmosphere-only (GA7) free-running simulation, and (c, f, i) GloSea5 hindcasts (with start dates in May), for (a–c) June, (d–f) July, and (g–i) August. Shadings in (a, d, g) denote climatological precipitation (GPCP), while in (b, e, h) and (c, f, i) denote model bias.

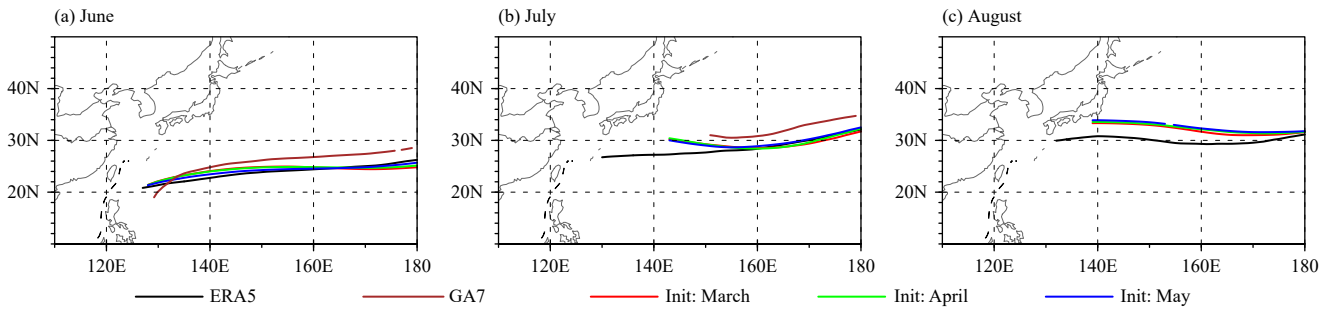

Fig. 3. Climatological WNPSH ridge line in (a) June, (b) July, and (c) August from the ERA5 (black line), MetUM atmosphere-only (GA7) free-running simulation (brown line), and GloSea5 hindcasts with initial forecast dates in March (red line), April (green line), and May (blue line), respectively.

ively high prediction skill in July needs further investigation. GloSea5 also shows significant prediction skill for the interannual variation in the latitudinal position of the WNPSH ridge line in JJA. The correlation coefficient between the observations and model ensemble mean is 0.73 with start dates in March, passing a reliability test at the 0.01 significance level (Fig. 4b). The hindcast results for the ridge line at all lead times show a systematic northward displacement of about 1°–2°, compared with ERA5, smaller than most of the CMIP5 atmospheric gen-

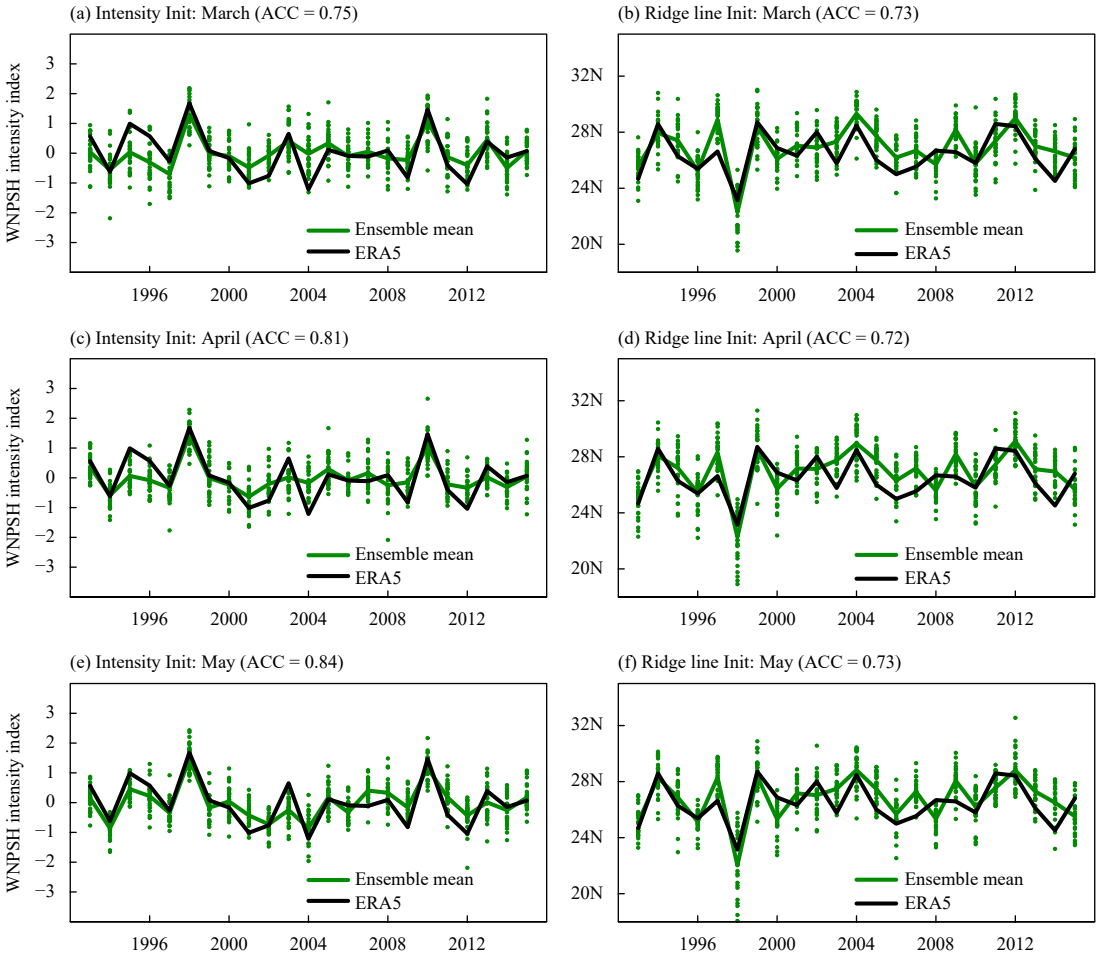

Fig. 4. Skills for predicting (a, c, e) the intensity of WNPSH using the index of Wang et al. (2013) based on the 850-hPa geopotential height in the box 15°–25°N, 115°–150°E and (b, d, f) the position of WNPSH ridge line in JJA. The anomaly correlation coefficient (ACC) is between predicted WNPSH indices in JJA from GloSea5 (green) and those from ERA5 (black) for hindcast start dates in March, April, and May (1st, 9th, 17th, and 25th of the months). The ACC values given in the panel headings represent the correlations between the ensemble mean and ERA5.

Table 1. Skill for predicting the intensity of the WNPSH: anomaly correlation coefficients between the predicted WNPSH index in June, July, and August (JJA) from GloSea5 and those from ERA5 for the hindcast start dates in March, April, and May (1st, 9th, 17th, and 25th of the months)

Month	March	April	May
June	0.41	0.43	0.71
July	0.70	0.70	0.64
August	0.44	0.67	0.65

eral circulation model results (Dong et al., 2017).

The skills in 1998 and 2010 are significantly higher than in other years for the prediction of the intensity of WNPSH. The predicted WNPSH intensity is in close agreement with the observations. Both of the two years are in the decaying phase of El Niño. Previous studies have indicated that the atmospheric circulation and climate anomalies over the WNP region show a higher predictability during El Niño decaying summers (Wang et al., 2000; Xie et al., 2009). The latitudinal position of the ridge line in 1998 and 2010 is also well predicted.

4. Predictability of WNPSH associated with different phases of ENSO

As the most significant interannual signal in the air–sea coupled system, ENSO has a great influence on drought and flood disasters over East Asia through its impact on the evolution of the lower tropospheric cyclone/anticyclone and the intensity and displacement of the WNPSH (Wang et al., 2000; Huang et al., 2012). Studies have shown that the seasonal predictability of the variability of summer climate in the WNP mainly arises from the remote teleconnection associated with ENSO forcing, monsoon–ocean interactions in the TIO, and local atmosphere–ocean coupling (Wang et al., 2009; Chowdary et al., 2010; Kosaka et al., 2013). To assess systematic characteristics of the model bias under the

background of different external forcing and to investigate possible causes of the model bias in simulation of WNPSH, we composited the anomalies of 500-hPa geopotential height, 850-hPa wind, integrated moisture flux, and precipitation in summer from both the observations and GloSea5 hindcast dataset with start dates in May based on years in different phases of ENSO.

To determine the ENSO phase of a particular summer, we divided the entire 23 years from 1993 to 2015 into 5 categories: El Niño decaying, La Niña decaying, El Niño developing, La Niña developing, and neutral years (Table 2). The start/end, persistence, and intensity of ENSO events were determined by the Niño3.4 index, which was defined as the mean SSTA in the Niño3.4 region (5°S–5°N, 120°–170°W; Trenberth and Stepaniak, 2001). An ENSO event was identified once the absolute value of the 3-month moving average of the Niño3.4 index exceeded 0.5°C and persisted for more than 5 months, with the Niño3.4 index greater than or equal to 0.5°C defined as an El Niño event and the Niño3.4 index less than or equal to −0.5°C as a La Niña event (Ren et al., 2018). As a result of the phase-locking phenomenon, ENSO events tend to peak in the boreal winter (Neelin et al., 2000). For instance, a canonical El Niño event develops during the boreal summer, peaks during the early winter, and decays in the ensuing spring (Xie et al., 2009). The developing or decaying years of El Niño/La Niña events were defined by the summers before or after the mature phase of the El Niño/La Niña event. According to our classification, 1995, 1998, 2007, and 2010 were both El Niño decaying and La Niña developing years and were therefore included in both types of event (Table 2). The year 1999 was a La Niña persisting year and was not included in the five types. The remaining years were classified as neutral years.

The model captured the summer WNPSH anomalies well during most of the ENSO phases from 1993 to 2015, except for La Niña decaying and neutral summers. Anticyclonic anomalies in the 850-hPa wind field and positive geopotential height anomalies were seen over the WNP in both ERA5 and the GloSea5 hindcasts during El Niño decaying summers (Figs. 5a, b), whereas the intensity of the anomalous anticyclone in GloSea5 was weak compared with the reanalysis results, indicating a negative bias in the model prediction of the intensity of the WNPSH. The negative rainfall anomalies over the WNP were predicted well by the model. However, the rainfall anomalies between the observations and the model showed a significant discrepancy in southern China, where they were below normal in the observations and above normal in the model predictions.

Table 2. Classification of the 1993–2015 summers according to the phase of ENSO

ENSO phase	Number of years	Year
El Niño decaying	6	1995, 1998, 2003, 2005, 2007, 2010
La Niña decaying	6	1996, 2000, 2001, 2008, 2011, 2012
El Niño developing	7	1994, 1997, 2002, 2004, 2006, 2009, 2015
La Niña developing	4	1995, 1998, 2007, 2010
Neutral	3	1993, 2013, 2014

ENSO is generally classified into two types based on the spatial patterns of the SSTAs: the East Pacific El Niño and the central Pacific El Niño (Fu and Fletcher, 1985; Ashok et al., 2007; Ren and Jin, 2011). Previous studies have shown that the formation mechanism, evolution process, and climate response of the two types of ENSO are different. In contrast to the influence of the canonical East Pacific El Niño, summer rainfall from the Huai River to Yellow River is above normal in central Pacific El Niño decaying years, whereas the rainfall is below normal in southern China as a result of different atmospheric responses (Feng et al., 2011). Owing to the increased frequency of the central Pacific El Niño in the last few decades (Ren et al., 2020), the observed composite rainfall anomaly showed the central Pacific El Niño responses, whereas the GloSea5 prediction was unable to capture these spatial characteristics (Figs. 6a, b).

The intensity and location of cyclonic anomalies over the WNP and the weak WNPSH were captured well for the El Niño developing summers (Figs. 5e, f). However, there were anticyclonic wind anomalies over the seas east of Japan in the reanalysis dataset, which were not predicted by GloSea5. The positive rainfall anomalies over the WNP were predicted well, except in South China (Figs. 6e, f). GloSea5 also produced the anticyclonic wind anomalies and associated strong WNPSH in La Niña developing summers well (Figs. 5g, h). The negative rainfall anomalies over the WNP, the intensified water vapor transport, and the accompanying increased precipitation in the Yangtze River valley were all predicted well (Figs. 6g, h).

The prediction skill for both the atmospheric circulation and rainfall anomalies was relatively low in La Niña decaying and neutral summers. For La Niña decaying summers, negative geopotential height anomalies and cyclonic wind anomalies could be found over the South China Sea and the Philippines in the ERA5 reanalysis dataset, whereas the anomalies in geopotential height and wind fields were particularly weak in the GloSea5 hindcasts (Figs. 5c, d). The rainfall anomalies and water va-

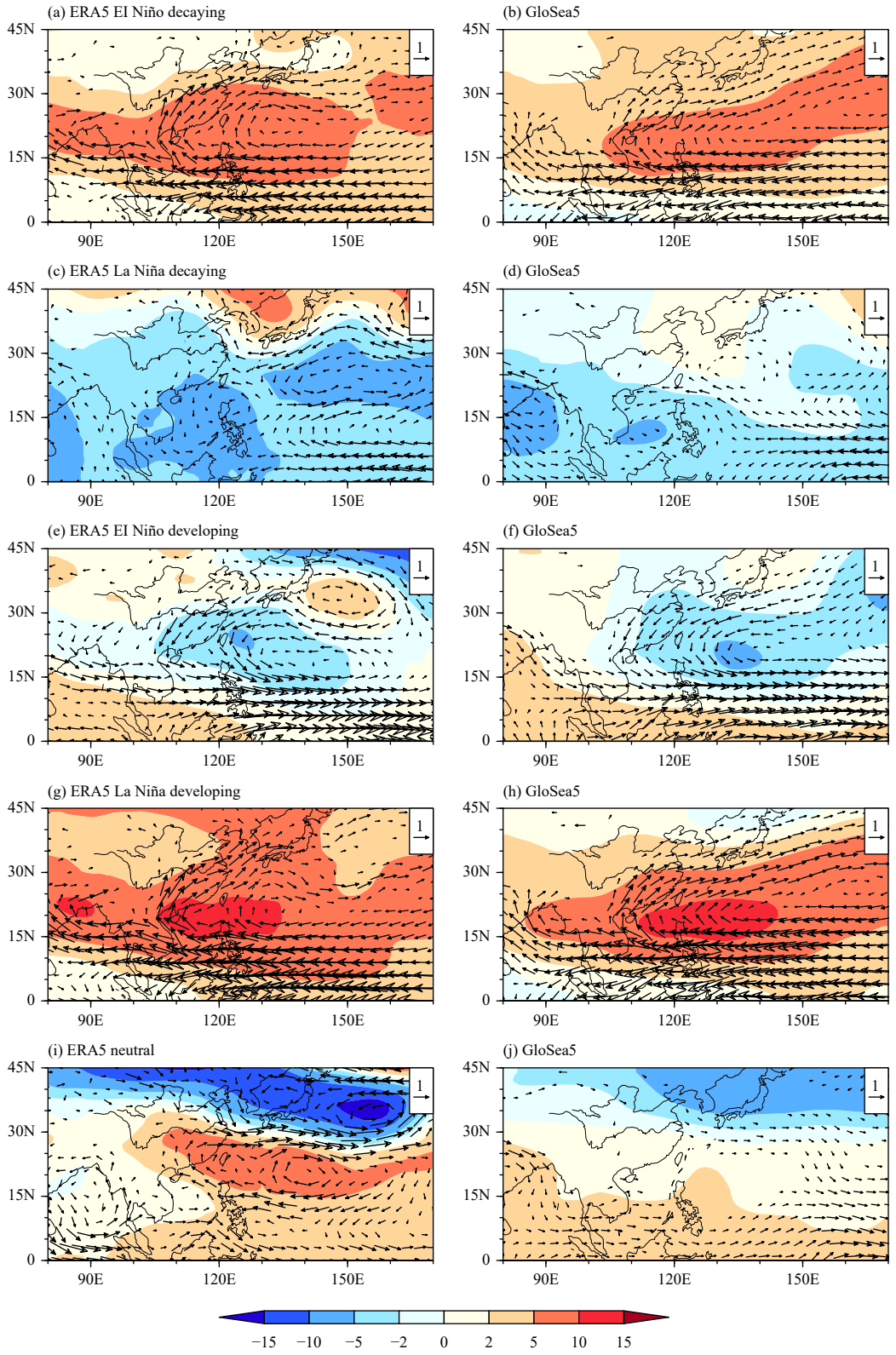

Fig. 5. Composite anomalies of the 500-hPa geopotential height (shading; gpm) and 850-hPa winds (vector; m s^{-1}) in JJA based on changing ENSO conditions. Left column: ERA5; right column: GloSea5, with start dates in May.

por transport also showed significant biases between the reanalysis data and the model output (Figs. 6c, d). Possible reasons for the low prediction skill include weak atmospheric circulation anomalies compared with other

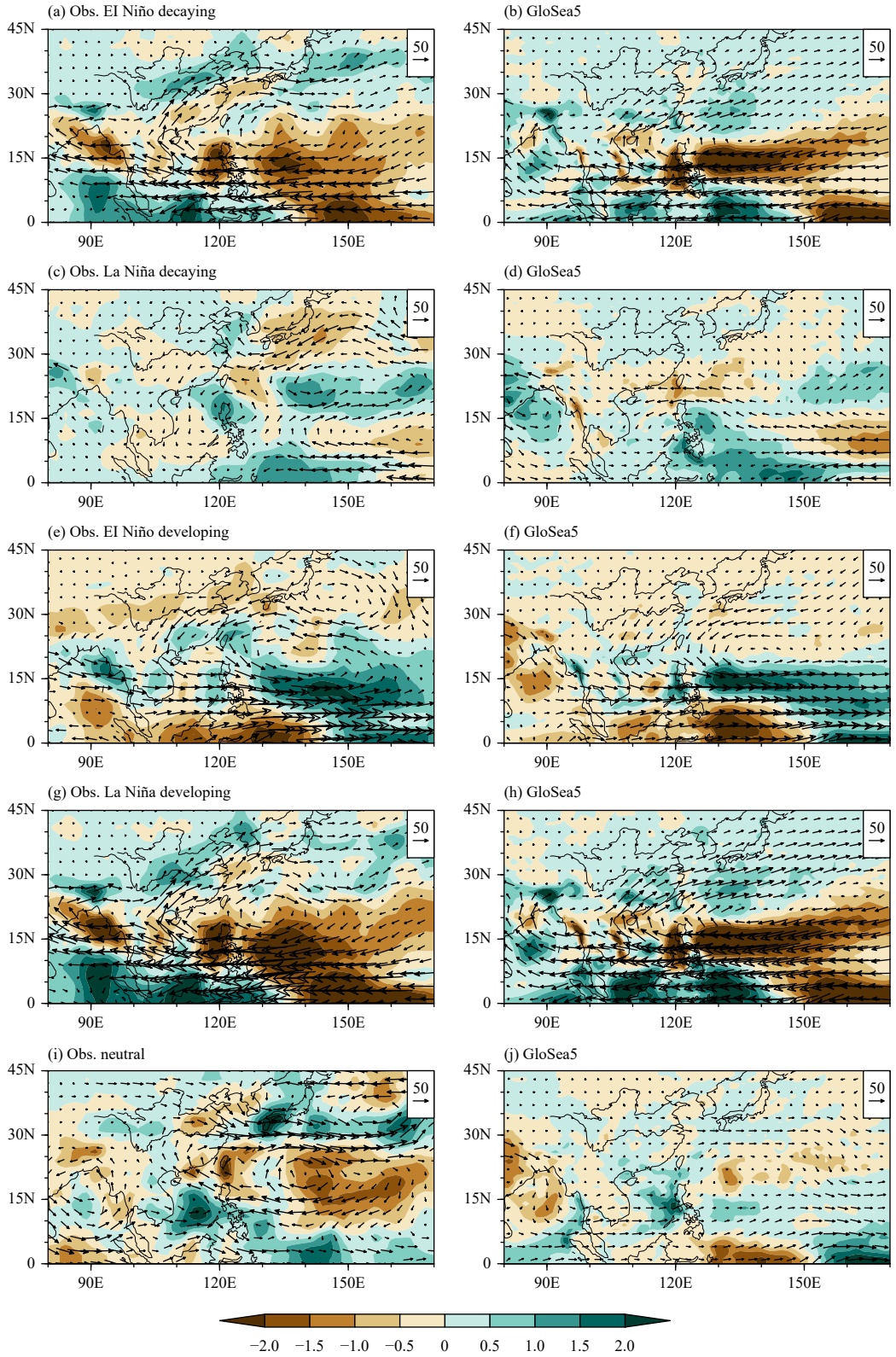

Fig. 6. Composite anomalies of the vertically integrated moisture flux (vector; kg m^{-1} s^{-1}) and precipitation (shading; mm day^{-1}) in JJA based on changing ENSO conditions. Left column: observations; right column: GloSea5, with start dates in May.

phases of ENSO (Li et al., 2014) and the increased frequency of tropical cyclones during La Niña decaying summers (Chan, 2000), which limit the model's ability to decently describe the characteristics of the large-scale

circulation over the WNP and East Asia. Analysis of observational data and model simulations indicated that the response of EASM's predictability to El Niño and La Niña events is asymmetrical, with a lower potential predictability under La Niña forcing than El Niño forcing (Li et al., 2018).

Among the ENSO neutral years, both the 1993 and 2013 summers showed intensified WNPSH and anticyclonic anomalies over the WNP. In 1993, the Niño3.4 index exceeded 0.5°C from March to June, lasting for 4 months, but did not form an El Niño event (Ren et al., 2018). However, the atmospheric circulation showed a significant response to the warm phase of ENSO, with weakened convection, low-level anticyclonic wind anomalies around the Philippines, and an intensified WNPSH (Chen, 1994). In summer 2013, the extreme intensity and the northward and westward extension of the WNPSH were mainly caused by the unusually high SSTs in the equatorial western Pacific, the westerly wind drift region, and the Kuroshio Current area, suggesting a positive feedback of local air–sea interactions (Li et al., 2014; Zou et al., 2015). The model was unable to capture this positive feedback under the background of ENSO neutral years (Figs. 5i, j). An easterly anomaly was found near 15°N in the composite anomalies of the integrated moisture flux over the WNP, whereas GloSea5 showed westerly anomalies (Figs. 6i, j).

The climatological cyclonic anomalies and negative geopotential height bias over the WNP region in GloSea5 were mainly attributed to the weak WNP anomalous anticyclone (WNPAC) simulated during the El Niño decaying phase. It is suggested in Section 3.1 that the atmospheric model biases over the WNP might be exacerbated by air–sea interactions. To investigate the role of SSTAs in the formation of the coupled model biases, we further analyzed the influence of the SSTAs in different oceanic regions on the summer WNPSH based on ERA5 and GloSea5 hindcast datasets.

Previous studies have shown that the interannual variation of WNPSH is influenced by not only local air–sea interactions, but also remote SSTAs (He et al., 2015). Several oceanic regions have been found to be responsible for the interannual variability of WNPSH in summer, among which the CEP and TIO are two key oceanic regions (Qian et al., 2018). The canonical El Niño peaks during the boreal winter, but its influence on WNPSH via the WNPAC persists into the following summer through the Indian Ocean capacitor mechanism (Xie et al., 2016). The positive feedback between the WNPAC and the underlying dipolar SSTAs over the WNP and TIO also contributes to the maintenance of the WNPAC (Wang et al., 2013).

To investigate the source of the prediction skill for the WNPSH and its relationship to SSTAs in different oceanic regions in both the observations and model hindcasts with different initial dates, we regressed the WNPSH intensity index onto the SSTA of the previous winter (DJF). Figure 7 shows that changes in the intensity of WNPSH per unit of SSTA were the strongest in the TIO in both the reanalysis and GloSea5 hindcasts. Over-

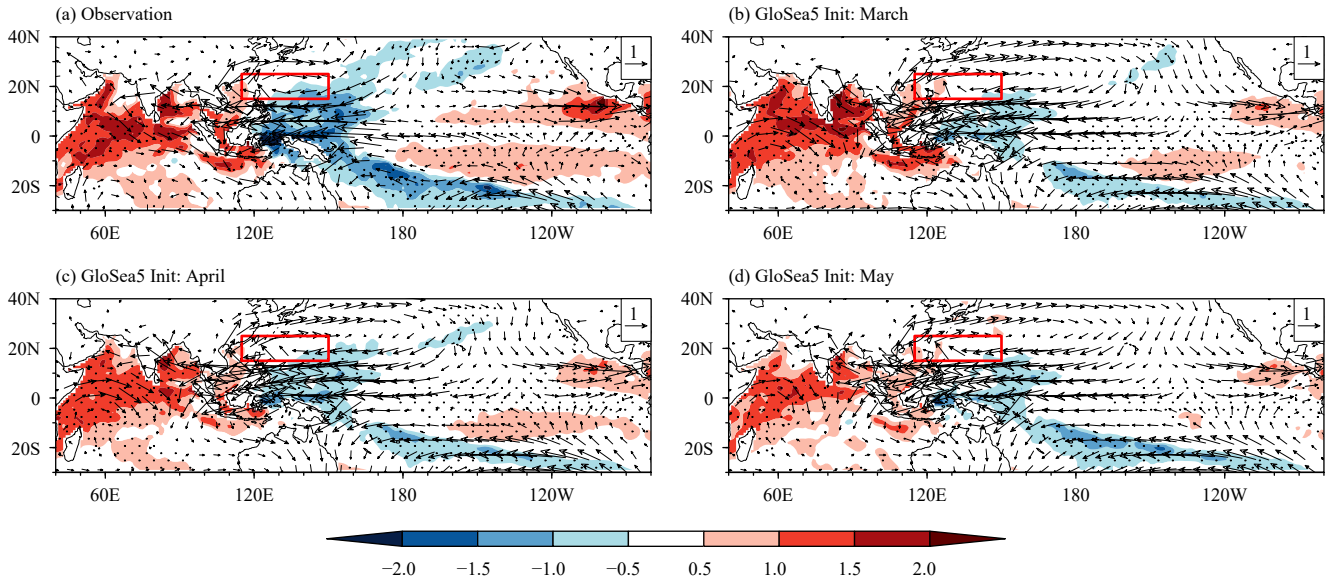

Fig. 7. Regression of the WNPSH intensity index (normalized, dimensionless) on the SSTAs in the previous winter (DJF; shading; K^{-1}) and regression of the 850-hPa winds in JJA on the WNPSH (vector; m s^{-1}) from the (a) observation and GloSea5 hindcasts initialized in (b) March, (c) April, and (d) May.

all, the relationship to the previous winter SSTAs weakened in both the CEP and TIO with shorter forecast lead times. Another notable difference between the model hindcast and reanalysis was the weakened negative SSTAs over the WNP, with a decreased gradient between the tropical western Pacific and the TIO (He and Zhou, 2015). The contributions from the negative SSTAs in the WNP, which combine with the positive SSTAs in the South China Sea and the TIO to promote easterly anomalies, were weaker in the model hindcast than in the reanalysis, resulting in a weaker easterly anomaly contributing to the weak anomalous anticyclone in the WNP, compared with the reanalysis. Although the relationship between the intensity of WNPSH and the SSTAs was stronger in the TIO than in the CEP, the typical interannual variations of SST in the TIO were far smaller, so there was a stronger contribution from the CEP to the interannual variation of the intensity of WNPSH, compared with that from the TIO. After scaling by the standard deviation of the SSTA, contribution of the SSTAs in the CEP was more significant than that in the TIO (Fig. 8a). GloSea5 was unable to simulate this relative contribution of the SSTAs from different oceanic regions, showing an almost equivalent importance of the CEP and TIO (Figs. 8b–d). The influence of the DJF SSTAs on the WNPSH in the following summer in the GloSea5 hindcasts decreased with the lead time from March to May.

The meridional width of the ENSO simulated in GloSea5 was limited, compared with the observation (Fig. 8). Studies have shown that the narrow bias in the simulated width of the ENSO is mainly due to a systematic bias in the weak trade winds, which leads to weak ocean meridional currents (Zhang and Jin, 2012; Zhang et al., 2013) associated with a bias toward short ENSO periods. Previous modeling results have also suggested that El Niño events with a short decay phase lead to significant WNPAC anomalies in the following summer (Chen et al., 2012) and that the WNPAC serves as an important atmospheric system in the interaction between ENSO and WNPSH. Therefore, the limited meridional width of the ENSO simulated in GloSea5 compared with the observation (Fig. 8) might also influence the predictability of the WNPSH.

5. Summary and discussion

Both a free-running, multi-decadal atmosphere-only MetUM simulation and an initialized, multi-year GloSea5 hindcast ensemble showed systematic biases in the mean circulation of the WNPSH in boreal summer. The biases were manifested in (1) a stronger westerly circulation over the Indochina Peninsula, the South China Sea, and the Philippine Sea; (2) negative geopotential height anomalies over the WNP; and (3) cyclonic anomalies in the 850-hPa winds and water vapor transport, indicating a weakening and eastward-shifted WNPSH. The systematic biases were more significant in the coupled GloSea5 dataset than in the MetUM free-running dataset, and they became larger as the lead time of prediction increased. The position of the climatological ridge line of the WNPSH in the GloSea5 simulation showed a northward dis-

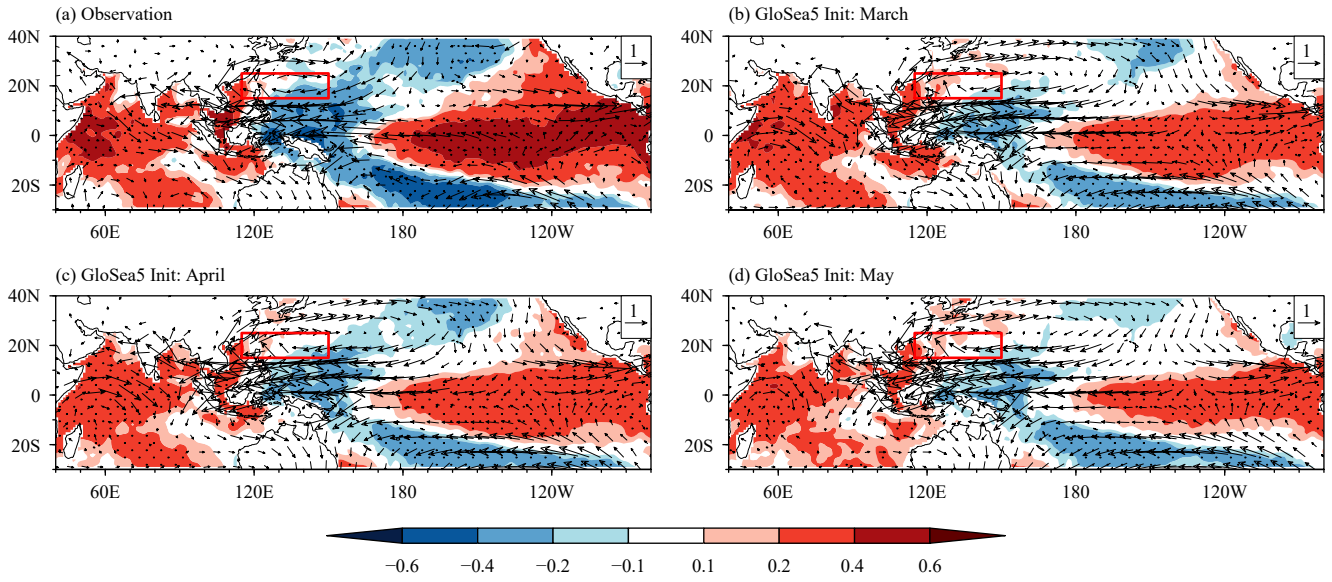

Fig. 8. As in Fig. 7, but for the regression coefficients of WNPSH against SSTAs scaled by the interannual standard deviation of the SSTA from the previous winter [considering the change in WNPSH index (dimensionless) contributed by a typical interannual SSTA at each point].

placement relative to the ERA5 reanalysis dataset, especially in July and August.

The interannual variability in the intensity of the WNPSH in boreal summer was captured well. Both the intensity and latitudinal position of the ridge line of the summer mean WNPSH showed a robust predictive skill in the GloSea5 hindcast with a lead time of up to three months. The correlation coefficient between the ERA5 reanalysis dataset and the GloSea5 ensemble mean with start dates in March for the intensity of the WNPSH was as high as 0.75 and the prediction skill increased as the lead time of the forecast decreased. The intensity of the WNPSH was also predictable with a high skill on the monthly basis, consistent with the results of Martin et al. (2020) for the EASM index of Wang et al. (2008).

Comparative analysis showed that the overall patterns of the atmospheric circulation and precipitation over the WNP were well simulated in GloSea5, although there were still some biases, especially associated with different ENSO phases. The model captured the summer WNPSH anomalies well during most of the ENSO phases, except in the La Niña decaying and neutral summers. Possible reasons for the low prediction skill include the weak atmospheric circulation anomalies during La Niña decaying and neutral summers, an increase in the number of tropical cyclones, and the limited capability of the model to simulate different atmospheric responses to El Niño events in eastern and central Pacific and local air–sea interactions. The positive anomalies of geopotential height over the WNP and WNPAC during El Niño decaying summers in GloSea5 were weak compared with the observations. GloSea5 was also unable to capture the intensified WNPSH and anticyclonic anomalies over the WNP in ENSO neutral years, in association with the local air–sea interaction. Both the weakened atmospheric response to ENSO and the under-represented local air–sea interaction led to the model bias in climatology of the WNPSH in the GloSea5 simulation.

Contributions of the SSTAs in different oceanic regions in the formation of model bias were also investigated. Regression analysis showed a weakened negative SSTA over the WNP in GloSea5, which decreased the gradient between the tropical western Pacific and the TIO, resulting in a weaker easterly anomaly, and contributed to the weak anomalous anticyclone in the WNP and the weakened WNPSH compared with the reanalysis dataset. The weakening of the relationship between the model and the simulated summer WNPSH and SSTA of preceding winter for later initialization dates might be attributed to the signal driven by SSTs in DJF decreasing as the initial dates of the model became further from the winter. In observations, the contributions from the variations of the SSTAs in the TIO were smaller than those in the CEP. However, variations of SSTAs in both TIO and CEP contributed almost equivalently in GloSea5.

The presence of significant skills in GloSea5 hindcasts for prediction of the position and intensity of the WNPSH on seasonal timescales and for subseasonal prediction of the intensity of the WNPSH, despite the model biases, underpins existing climate services such as the seasonal forecast of rainfall in the Yangtze River basin (Bett et al., 2018). It also offers the potential for further development of these climate services—for example, by using the dynamic forecast of the EASM index of Wang et al. (2008), which captures the low-level circulation associated with the WNPSH. Bett et al. (2020) showed that the seasonal-mean rainfall for the upper and mid–lower reaches of the Yangtze River basin can be forecast separately, with significant skill for lead times of up to three months. The presence of skill for predicting the intensity of the WNPSH on monthly timescales underpins the skill demonstrated for the prediction of June rainfall over the mid–lower Yangtze River basin (Martin et al., 2020) and offers the potential for further subseasonal prediction in the future.

Acknowledgments. We thank the anonymous reviewers for their helpful comments.

REFERENCES

Adler, R. F., M. R. P. Sapiano, G. J. Huffman, et al., 2018: The Global Precipitation Climatology Project (GPCP) monthly analysis (new version 2.3) and a review of 2017 global precipitation. *Atmosphere*, **9**, 138, doi: 10.3390/atmos9040138.

Ashok, K., S. K. Behera, S. A. Rao, et al., 2007: El Niño Modoki and its possible teleconnection. *J. Geophys. Res. Oceans*, **112**, C11007, doi: 10.1029/2006jc003798.

Best, M. J., M. Pryor, D. B. Clark, et al., 2011: The Joint UK Land Environment Simulator (JULES), model description—Part 1: Energy and water fluxes. *Geosci. Model Dev.*, **4**, 677–699, doi: 10.5194/gmd-4-677-2011.

Bett, P. E., H. E. Thornton, J. F. Lockwood, et al., 2017: Skill and reliability of seasonal forecasts for the Chinese energy sector. *J. Appl. Meteor.*, **56**, 3099–3114, doi: 10.1175/jamc-d-17-0070.1.

Bett, P. E., A. A. Scaife, C. F. Li, et al., 2018: Seasonal forecasts of the summer 2016 Yangtze River basin rainfall. *Adv. Atmos. Sci.*, **35**, 918–926, doi: 10.1007/s00376-018-7210-y.

Bett, P. E., N. Martin, A. A. Scaife, et al., 2020: Seasonal rainfall forecasts for the Yangtze River basin of China in summer 2019 from an improved climate service. *J. Meteor. Res.*, **34**, 904–916, doi: 10.1007/s13351-020- 0049-z.

Bowler, N. E., A. Arribas, S. E. Beare, et al., 2009: The local ETKF and SKEB: Upgrades to the MOGREPS short-range ensemble prediction system. *Quart. J. Roy. Meteor. Soc.*, **135**, 767–776, doi: 10.1002/qj.394.

Camp, J., M. Roberts, C. MacLachlan, et al., 2015: Seasonal forecasting of tropical storms using the Met Office GloSea5 seasonal forecast system. *Quart. J. Roy. Meteor. Soc.*, **141**, 2206–2219, doi: 10.1002/qj.2516.

Chan, J. C. L., 2000: Tropical cyclone activity over the western North Pacific associated with El Niño and La Niña events. *J. Climate*, **13**, 2960–2972, doi: 10.1175/1520-0442(2000)013<2960:tcaotw>2.0.co;2.

Chen, G. Y., 1994: General circulation over Northern Hemisphere in 1993 and their impact on the weather and climate in China. *Meteor. Mon.*, **20**, 23–26. (in Chinese)

Chen, R. D., Z. P. Wen, R. Y. Lu, et al., 2019: Causes of the extreme hot midsummer in Central and South China during 2017: Role of the western tropical Pacific warming. *Adv. Atmos. Sci.*, **36**, 465–478, doi: 10.1007/s00376-018-8177-4.

Chen, W., J.-K. Park, B.-W. Dong, et al., 2012: The relationship between El Niño and the western North Pacific summer climate in a coupled GCM: Role of the transition of El Niño decaying phases. *J. Geophys. Res. Atmos.*, **117**, D12111, doi: 10.1029/2011JD017385.

Chou, C., J. Y. Tu, and J. Y. Yu, 2003: Interannual variability of the western North Pacific summer monsoon: Differences between ENSO and non-ENSO years. *J. Climate*, **16**, 2275–2287, doi: 10.1175/2761.1.

Chowdary, J. S., S. P. Xie, J. Y. Lee, et al., 2010: Predictability of summer Northwest Pacific climate in 11 coupled model hindcasts: Local and remote forcing. *J. Geophys. Res. Atmos.*, **115**, D22121, doi: 10.1029/2010jd014595.

Dee, D. P., S. M. Uppala, A. J. Simmons, et al., 2011: The ERA-Interim reanalysis: Configuration and performance of the data assimilation system. *Quart. J. Roy. Meteor. Soc.*, **137**, 553–597, doi: 10.1002/qj.828.

Dong, X., F.-X. Fan, R.-P. Lin, et al., 2017: Simulation of the western North Pacific subtropical high in El Niño decaying summers by CMIP5 AGCMs. *Atmos. Ocean. Sci. Lett.*, **10**, 146–155, doi: 10.1080/16742834.2017.1272404.

Feng, J., W. Chen, C.-Y. Tam, et al., 2011: Different impacts of El Niño and El Niño Modoki on China rainfall in the decaying phases. *Int. J. Climatol.*, **31**, 2091–2101, doi: 10.1002/joc.2217.

Fu, Z. B., and J. Fletcher, 1985: Two patterns of equatorial warming associated with El Niño. *Chinese Sci. Bull.*, **30**, 1360–1364.

Gao, H., T. Ding, and W. J. Li, 2017: The three-dimension intensity index for western Pacific subtropical high and its link to the anomaly of rain belt in eastern China. *Chinese Sci. Bull.*, **62**, 3643–3654, doi: 10.1360/N972017-00280. (in Chinese)

Hardiman, S. C., N. J. Dunstone, A. A. Scaife, et al., 2018: The asymmetric response of Yangtze River basin summer rainfall to El Niño/La Niña. *Environ. Res. Lett.*, **13**, 024015, doi: 10.1088/1748-9326/aaa172.

He, C., and T. J. Zhou, 2014: The two interannual variability modes of the western North Pacific subtropical high simulated by 28 CMIP5-AMIP models. *Climate Dyn.*, **43**, 2455–2469, doi: 10.1007/s00382-014-2068-x.

He, C., and T. J. Zhou, 2015: Responses of the western North Pacific subtropical high to global warming under RCP4.5 and RCP8.5 scenarios projected by 33 CMIP5 models: The dominance of tropical Indian Ocean–tropical western Pacific SST gradient. *J. Climate*, **28**, 365–380, doi: 10.1175/jcli-d-13-00494.1.

He, C., T. J. Zhou, and B. Wu, 2015: The key oceanic regions responsible for the interannual variability of the western North Pacific subtropical high and associated mechanisms. *J. Meteor. Res.*, **29**, 562–575, doi: 10.1007/s13351-015-5037-3.

He, C., A. L. Lin, D. J. Gu, et al., 2018: Using eddy geopotential height to measure the western North Pacific subtropical high in a warming climate. *Theor. Appl. Climatol.*, **131**, 681–691, doi: 10.1007/s00704-016-2001-9.

Hoffmann, L., G. Günther, D. Li, et al., 2019: From ERA-Interim to ERA5: The considerable impact of ECMWF's next-generation reanalysis on Lagrangian transport simulations. *Atmos. Chem. Phys.*, **19**, 3097–3124, doi: 10.5194/acp-19-3097-2019.

Hong, J.-S., S.-W. Yeh, and K.-H. Seo, 2018: Diagnosing physical mechanisms leading to pure heat waves versus pure tropical nights over the Korean Peninsula. *J. Geophys. Res. Atmos.*, **123**, 7149–7160, doi: 10.1029/2018JD028360.

Huang, R. H., J. L. Chen, L. Wang, et al., 2012: Characteristics, processes, and causes of the spatio-temporal variabilities of the East Asian monsoon system. *Adv. Atmos. Sci.*, **29**, 910–942, doi: 10.1007/s00376-012-2015-x.

Kosaka, Y., S.-P. Xie, N.-C. Lau, et al., 2013: Origin of seasonal predictability for summer climate over the northwestern Pacific. *Proc. Natl. Acad. Sci. USA*, **110**, 7574–7579, doi: 10.1073/pnas.1215582110.

Lee, E.-J., S.-W. Yeh, J.-G. Jhun, et al., 2006: Seasonal change in anomalous WNPSH associated with the strong East Asian summer monsoon. *Geophys. Res. Lett.*, **33**, L21702, doi: 10.1029/2006GL027474.

Li, B. S., R. Q. Ding, J. P. Li, et al., 2018: Asymmetric response of predictability of East Asian summer monsoon to ENSO. *SOLA*, **14**, 52–56, doi: 10.2151/sola.2018-009.

Li, C. F., R. Y. Lu, and B. W. Dong, 2012: Predictability of the western North Pacific summer climate demonstrated by the coupled models of ENSEMBLES. *Climate Dyn.*, **39**, 329–346, doi: 10.1007/s00382-011-1274-z.

Li, C. F., R. Y. Lu, and B. W. Dong, 2014: Predictability of the western North Pacific summer climate associated with different ENSO phases by ENSEMBLES multi-model seasonal forecasts. *Climate Dyn.*, **43**, 1829–1845, doi: 10.1007/s00382-013-2010-7.

Li, C. F., A. A. Scaife, R. Y. Lu, et al., 2016: Skillful seasonal prediction of Yangtze River valley summer rainfall. *Environ. Res. Lett.*, **11**, 094002, doi: 10.1088/1748-9326/11/9/094002.

Liu, Y. M., J. L. Hong, C. Liu, et al., 2013: Meiyu flooding of Huaihe River valley and anomaly of seasonal variation of subtropical anticyclone over the western Pacific. *Chinese J. Atmos. Sci.*, **37**, 439–450, doi: 10.3878/j.issn.1006-9895.2012.12313. (in Chinese)

Liu, Y. Y., W. J. Li, W. X. Ai, et al., 2012: Reconstruction and application of the monthly western Pacific subtropical high indices. *J. Appl. Meteor. Sci.*, **23**, 414–423, doi: 10.3969/j.issn.1001-7313.2012.04.004. (in Chinese)

Liu, Y. Y., W. J. Li, J. Q. Zuo, et al., 2014: Simulation and projection of the western Pacific subtropical high in CMIP5 models. *J. Meteor. Res.*, **28**, 327–340, doi: 10.1007/s13351-014-3151-2.

Lockwood, J. F., H. E. Thornton, N. Dunstone, et al., 2019: Skilful seasonal prediction of winter wind speeds in China. *Cli-*

mate Dyn., **53**, 3937–3955, doi: 10.1007/s00382-019-04763-8.

Lu, B., A. A. Scaife, N. Dunstone, et al., 2017: Skillful seasonal predictions of winter precipitation over southern China. *Environ. Res. Lett.*, **12**, 074021, doi: 10.1088/1748-9326/aa739a.

Lu, R. Y., and B. W. Dong, 2001: Westward extension of North Pacific subtropical high in summer. *J. Meteor. Soc. Japan*, **79**, 1229–1241, doi: 10.2151/jmsj.79.1229.

Lu, R. Y., Y. Li, and C. S. Ryu, 2008: Relationship between the zonal displacement of the western Pacific subtropical high and the dominant modes of low-tropospheric circulation in summer. *Prog. Nat. Sci.*, **18**, 161–165, doi: 10.1016/j.pnsc.2007.07.009.

MacLachlan, C., A. Arribas, K. A. Peterson, et al., 2015: Global Seasonal forecast system version 5 (GloSea5): A high-resolution seasonal forecast system. *Quart. J. Roy. Meteor. Soc.*, **141**, 1072–1084, doi: 10.1002/qj.2396.

Martin, G. M., A. Chevuturi, R. E. Comer, et al., 2019: Predictability of South China Sea summer monsoon onset. *Adv. Atmos. Sci.*, **36**, 253–260, doi: 10.1007/s00376-018-8100-z.

Martin, G. M., N. J. Dunstone, A. A. Scaife, et al., 2020: Predicting June mean rainfall in the middle/lower Yangtze River basin. *Adv. Atmos. Sci.*, **37**, 29–41, doi: 10.1007/s00376-019-9051-8.

Megann, A., D. Storkey, Y. Aksenov, et al., 2014: GO5.0: The joint NERC–Met Office NEMO global ocean model for use in coupled and forced applications. *Geosci. Model Dev.*, **7**, 1069–1092, doi: 10.5194/gmd-7-1069-2014.

Neelin, J. D., F.-F. Jin, and H.-H. Syu, 2000: Variations in ENSO phase locking. *J. Climate*, **13**, 2570–2590, doi: 10.1175/1520-0442(2000)013<2570:viepl>2.0.co;2.

Niñomiya, K., and C. Kobayashi, 1998: Precipitation and moisture balance of the Asian summer monsoon in 1991. Part Ⅰ: Precipitation and major circulation systems. *J. Meteor. Soc. Japan*, **76**, 855–877, doi: 10.2151/jmsj1965.76.6_855.

Niñomiya, K., and C. Kobayashi, 1999: Precipitation and moisture balance of the Asian summer monsoon in 1991. Part Ⅱ: Moisture transport and moisture balance. *J. Meteor. Soc. Japan*, **77**, 77–99, doi: 10.2151/jmsj1965.77.1_77.

Qian, D. L., Z. Y. Guan, and W. Y. Tang, 2018: Joint impacts of SSTA in tropical Pacific and Indian oceans on variations of the WPSH. *J. Meteor. Res.*, **32**, 548–559, doi: 10.1007/s13351-018-7172-0.

Rae, J. G. L., H. T. Hewitt, A. B. Keen, et al., 2015: Development of Global Sea Ice 6.0 CICE configuration for the Met Office global coupled model. *Geosci. Model Dev.*, **8**, 2221–2230, doi: 10.5194/gmdd-8-2529-2015.

Rayner, N. A., D. E. Parker, E. B. Horton, et al., 2003: Global analyses of sea surface temperature, sea ice, and night marine air temperature since the late nineteenth century. *J. Geophys. Res. Atmos.*, **108**, 4407, doi: 10.1029/2002jd002670.

Ren, H.-L., and F.-F. Jin, 2011: Niño indices for two types of ENSO. *Geophys. Res. Lett.*, **38**, L04704, doi: 10.1029/2010gl046031.

Ren, H.-L., B. Lu, J. H. Wan, et al., 2018: Identification standard for ENSO events and its application to climate monitoring and prediction in China. *J. Meteor. Res.*, **32**, 923–936, doi: 10.1007/s13351-018-8078-6.

Ren, H.-L., F. Zheng, J.-J. Luo, et al., 2020: A review of research on tropical air–sea interaction, ENSO dynamics, and ENSO prediction in China. *J. Meteor. Res.*, **34**, 43–62, doi: 10.1007/s13351-020-9155-1.

Tao, S. Y., Q. Y. Zhang, and S. L. Zhang, 2001: An observational study on the behavior of the subtropical high over the West Pacific in summer. *Acta Meteor. Sinica*, **59**, 747–758, doi: 10.11676/qxxb2001.078. (in Chinese)

Trenberth, K. E., and D. P. Stepaniak, 2001: Indices of El Niño evolution. *J. Climate*, **14**, 1697–1701, doi: 10.1175/1520-0442(2001)014<1697:lioeno>2.0.co;2.

Valcke, S., 2013: The OASIS3 coupler: A European climate modelling community software. *Geosci. Model Dev.*, **6**, 373–388, doi: 10.5194/gmd-6-373-2013.

Walters, D., I. Boutle, M. Brooks, et al., 2017: The Met Office unified model global atmosphere 6.0/6.1 and JULES global land 6.0/6.1 configurations. *Geosci. Model Dev.*, **10**, 1487–1520, doi: 10.5194/gmd-10-1487-2017.

Walters, D., A. J. Baran, I. Boutle, et al., 2019: The Met Office unified model global atmosphere 7.0/7.1 and JULES global land 7.0 configurations. *Geosci. Model Dev.*, **12**, 1909–1963, doi: 10.5194/gmd-12-1909-2019.

Wang, B., and Q. Zhang, 2002: Pacific–East Asian teleconnection. Part II: How the Philippine Sea anomalous anticyclone is established during El Niño development. *J. Climate*, **15**, 3252–3265, doi: 10.1175/1520-0442(2002)015<3252:peatpi>2.0.co;2.

Wang, B., R. G. Wu, and X. H. Fu, 2000: Pacific–East Asian teleconnection: How does ENSO affect East Asian climate? *J. Climate*, **13**, 1517–1536, doi: 10.1175/1520-0442(2000)013<1517:peathd>2.0.co;2.

Wang, B., Z. W. Wu, J. P. Li, et al., 2008: How to measure the strength of the East Asian summer monsoon. *J. Climate*, **21**, 4449–4463, doi: 10.1175/2008jcli2183.1.

Wang, B., J.-Y. Lee, I.-S. Kang, et al., 2009: Advance and prospectus of seasonal prediction: Assessment of the APCC/CliPAS 14-model ensemble retrospective seasonal prediction (1980–2004). *Climate Dyn.*, **33**, 97–117, doi: 10.1007/s00382-008-0460-0.

Wang, B., B. Q. Xiang, and J.-Y. Lee, 2013: Subtropical high predictability establishes a promising way for monsoon and tropical storm predictions. *Proc. Natl. Acad. Sci. USA*, **110**, 2718–2722, doi: 10.1073/pnas.1214626110.

Williams, K. D., C. M. Harris, A. Bodas-Salcedo, et al., 2015: The Met Office Global Coupled model 2.0 (GC2) configuration. *Geosci. Model Dev.*, **8**, 1509–1524, doi: 10.5194/gmdd-8-521-2015.

Wu, B., and T. J. Zhou, 2008: Oceanic origin of the interannual and interdecadal variability of the summertime western Pacific subtropical high. *Geophys. Res. Lett.*, **35**, L13701, doi: 10.1029/2008gl034584.

Xie, S. P., K. M. Hu, J. Hafner, et al., 2009: Indian Ocean capacitor effect on Indo–western Pacific climate during the summer following El Niño. *J. Climate*, **22**, 730–747, doi: 10.1175/2008jcli2544.1.

Xie, S. P., Y. Kosaka, Y. Du, et al., 2016: Indo–western Pacific ocean capacitor and coherent climate anomalies in post-ENSO summer: A review. *Adv. Atmos. Sci.*, **33**, 411–432, doi: 10.1007/s00376-015-5192-6.

Xue, F., X. Dong, and F. X. Fan, 2018: Anomalous western Pacific subtropical high during El Niño developing summer in

comparison with decaying summer. *Adv. Atmos. Sci.*, **35**, 360–367, doi: 10.1007/s00376-017-7046-x.

Yuan, Y., S. Yang, and Z. Q. Zhang, 2012: Different evolutions of the Philippine Sea anticyclone between the eastern and central Pacific El Niño: Possible effects of Indian Ocean SST. *J. Climate*, **25**, 7867–7883, doi: 10.1175/jcli-d-12-00004.1.

Yuan, Y., H. Gao, X. L. Jia, et al., 2016: Influences of the 2014–2016 super El Niño events on climate. *Meteor. Mon.*, **42**, 532–539. (in Chinese)

Yun, K.-S., S.-W. Yeh, and K.-J. Ha, 2013: Distinct impact of tropical SSTs on summer North Pacific high and western North Pacific subtropical high. *J. Geophys. Res. Atmos.*, **118**, 4107–4116, doi: 10.1002/jgrd.50253.

Zhang, R. H., A. Sumi, and M. Kimoto, 1999: A diagnostic study of the impact of El Niño on the precipitation in China. *Adv. Atmos. Sci.*, **16**, 229–241, doi: 10.1007/bf02973084.

Zhang, W. J., and F.-F. Jin, 2012: Improvements in the CMIP5 simulations of ENSO-SSTA meridional width. *Geophys. Res. Lett.*, **39**, L23704, doi: 10.1029/2012GL053588.

Zhang, W. J., F.-F. Jin, J.-X. Zhao, et al., 2013: On the bias in simulated ENSO SSTA meridional widths of CMIP3 models. *J. Climate*, **26**, 3173–3186, doi: 10.1175/JCLI-D-12-00347.1.

Zou, H. B., S. S. Wu, J. S. Shan, et al., 2015: Diagnostic study of the severe high temperature event over Mid–East China in 2013 summer. *Acta Meteor. Sinica*, **73**, 481–495, doi: 10.11676/qxxb2015.035. (in Chinese)

Tech & Copy Editor: Zhirong CHEN